Surface & Coatings Technology xxx (xxxx) xxx–xxx

Contents lists available at ScienceDirect

Surface & Coatings Technology

journal homepage: www.elsevier.com/locate/surfcoat

Effect of nozzle geometry on the gas dynamics and evaporation rates of Suspension High Velocity Oxy Fuel (SHVOF) thermal spray: A numerical investigation

S. Chadha, R. Jefferson-Loveday, T. Hussain*

Faculty of Engineering, University of Nottingham, Nottingham NG7 2RD, UK

ARTICLE INFO

Keywords:
SHVOF
HVSFS
Numerical modelling
Suspension thermal spray
Nozzle geometry
Volatile fraction

ABSTRACT

Thermally sprayed coatings formed from sub-micron or nanoparticles feedstock provide enhanced coating properties and Suspension High Velocity Oxy Fuel (SHVOF) thermal spray is a process that allows the deposition of dense coatings from fine particulates. However, in SHVOF thermal spray, submicron and nanoparticles are significantly influenced by fluctuations in the gas velocity and temperature field because of the turbulence and disturbance of the gas fields from the breakup of the suspension due to the small inertia of the particles. In this study, an ethanol suspension containing widely used engineering ceramic particles, TiO_2, with four different particle concentrations was considered 0, 10, 15 and 25 wt%. The aim of this paper was to model four nozzle geometries and to investigate the influence the nozzle geometry has on the gas flow and the evaporation rate at four particle concentrations. Comparing four nozzle geometries it is found that the gas exits the longer barrel nozzles at a high velocity; while the velocity in the free jet region beyond the shock diamonds is greater for the shorter nozzles. It is seen that the shorter the nozzle the higher the gas temperature in the free jet; which is due to the lower contact time of the gas with the cooled nozzle walls. This study also considered the effect the nozzle geometry has on the evaporation of the suspension. It was found that the longer the combustion chamber the lower the maximum evaporation rate. Moreover, higher particle concentrations result in evaporation commencing closer to the nozzle inlet due to the lower volatile fraction of the suspension.

1. Introduction

Thermal spraying allows for the deposition of particles onto a substrate to provide a protective coating against wear and corrosion. High velocity oxy-fuel (HVOF) thermal spray process allows the ability to produce dense coatings with low degradation and oxidation [1]. With the success of HVOF thermal spray industrial applications for wear resistant coatings grew exponentially. However, there are certain limitations with the conventional HVOF thermal spray process. One of these limitations arises from the inability to reduce particle size further to that of nano-feedstock sizes. Coatings formed from nanoparticles provide enhanced properties in contrast to standard powder particles (5–45 μm) [2,3].

Conventional powder feeders are ineffective when dealing with feedstock sizes below 5 μm. The development of Suspension High Velocity Oxy Fuel (SHVOF) thermal spray has allowed for effective handling of nanoparticle feedstock size which has enabled the deposition of coatings with a fine microstructure [2]. Modelling the SHVOF thermal spray process allows us to predict how a system will behave under a given set of operating conditions. From this one can conduct an investigation to predict the operating conditions that will produce the desired coating properties.

Within the last decade several studies have focused on modelling SHVOF thermal spray using the commercial CFD software Ansys Fluent (Canonsburg, Pennsylvania, USA). These studies have focused on initial droplet diameter, suspension feed rate, suspension composition, droplet breakup and substrate geometry to name a few. One such study by Tabbara and Gu [4] looked at injecting water droplets into the combustion chamber, to investigate the effect the initial parent droplet size has on the evaporation rate. The study focused on comparing droplet breakup and evaporation regimes for parent droplets ranging from 50 to 500 μm. This was one of the first computational investigations of SHVOF thermal spray and the aim of the paper was to investigate the effect of injecting a liquid into the combustion chamber has on the gas dynamics. The study neglected any influence of the particles and assumed that the properties of the suspension were constant which was

* Corresponding author.
E-mail address: Tanvir.Hussain@nottingham.ac.uk (T. Hussain).

https://doi.org/10.1016/j.surfcoat.2018.10.085
Received 14 March 2018; Received in revised form 4 June 2018; Accepted 27 October 2018

addressed in a later study [5]. A study by Mahrukh et al. [6] looked at the effect different injection and atomization models have on the droplet breakup and evaporation rates. The paper considered the injection of ethanol droplets into the combustion chamber accounting for varying particle concentrations. Three injection methods were implemented: a surface injection, a group injection and an effervescent injection. The angle of the suspension injection for the group and the effervescent injection were also modified and the results were compared to determine the optimum injection regime. This study also identified which angle would produce the most rapid droplet breakup and evaporation of suspension. Mahrukh et al. [5] considered the effect that the concentrations of solid nanoparticles within the suspension had on the SHVOF thermal spray process. Four concentrations were considered 0, 5, 15 and 25 wt% with respect to the total mass of the suspension and their effect on the gas dynamics, droplet breakup and evaporation were considered. This paper however assumed that for each of the four concentrations that the entire suspension was vaporized into gaseous ethanol and combusts which over predicts the temperature drop of the gas in the region of suspension vaporization for suspensions with high particle concentrations. The model also over predicts the temperature of the gas in the region of suspension combustion for suspensions with high particle concentrations.

There are many approaches one can take to modelling the SHVOF thermal spray process. Dongmo et al. looked at developing a model for the SHVOF thermal spray process [7]. One such model [7] looked at modelling the suspension as two separate discrete injections one for the liquid carrier and one for the nano-particles. Information on the particle trajectories, evaporation of suspension, particle velocity and temperature were obtained. Additional studies from this research group looked to determine the optimum injection angle of the suspension [8]. Jadidi et al. [9] investigated modelling the suspension using a coupled level set and volume of fraction model. This model was able to capture the primary droplet breakup which the DPM model is not able to do, this model however is significantly more computationally expensive than the DPM models currently used in SHVOF thermal spray modelling [9]. Taleby and Hossainpour investigated the effect of gas flow rate, suspension feed rate, droplet diameter and the droplet velocity [10]. Jadidi et al. investigated the effect the substrate geometry has on the particle dynamics [11,12]. The suspension is modelled as a multicomponent droplet (droplet comprising of multiple constituents). In the study by Jadidi et al. the specific heat was given by a mass weighted average of the two components as opposed to a volume weighted average of the two components. The volume approach aligns more closely with literature on a suspension droplet, the viscosity was also considered to be constant. The particle dynamics for two substrate geometries were investigated, a flat plate and a cylinder. A comprehensive review of the current literature in modelling SHVOF thermal spray is offered in the following reference [13]. It is clear from this work that a rigorous model for the suspension within SHVOF thermal spray has yet to be established as an effective model that couples the droplets and particles within the suspension has yet to be implemented.

There are numerous parameters such as the gas flow rate, suspension feed rate, suspension composition and the particle diameter to name a few which affect the gas dynamics and in-flight particle dynamics and therefore affect the overall quality of the coating. One factor that has received little attention and that plays a significant role on the SHVOF thermal spray is the nozzle geometry. In SHVOF thermal spray oxygen and fuel are injected into a mixing chamber and the premixed gasses enter the combustion chamber where the mixture undergoes combustion. The geometry of the nozzle is designed such that the gaseous products are accelerated to gas velocities exceeding 2000 m/s [14].

There are many nozzle geometries available from commercial SHVOF suppliers; however, there are no general consensuses as to which case each nozzle is best suited when it comes to suspension spray. Most nozzles were developed for conventional size HVOF powders, as opposed to suspensions. Understanding the effect that the nozzle geometry has on the gas temperature and velocity will allow for better control and predictability of coating properties.

This study aims to form a comprehensive comparative evaluation for four nozzle geometries in the SHVOF thermal spray process. This investigation compares the gas dynamics and evaporation rate for four nozzles to provide a basis of which an understanding can be formed on the suitability of nozzle geometry for a desired coating. This paper compares the gas pressure, velocity, temperature and droplet evaporation rates for a C_2H_5OH and TiO_2 based suspension injection.

2. Nozzle geometries

The nozzles in SHVOF thermal spray gun are comprised of a combustion chamber followed by a barrel. The region connecting the combustion chamber and the barrel is referred to as the throat within this study. The length of the combustion chamber and the total nozzle length are the main parameters that vary nozzle to nozzle. The nozzles follow a naming convention and the nozzle is named by three numbers, the numbers refer to the combustion chamber length, the total length and finally the barrel diameter respectively. For example, the 30-135-8 nozzle has a 30 mm long combustion chamber, a total length of 135 mm and a barrel diameter of 8 mm. The 0-78-8 nozzle has been named accordingly as this nozzle is a convergent barrel nozzle as opposed to a nozzle with a discrete combustion chamber as seen in the other three nozzles. The premixed fuel and oxygen were injected into the combustion chamber through an inlet with a diameter of 1 mm located at distance of 4 mm away from the axis of symmetry.

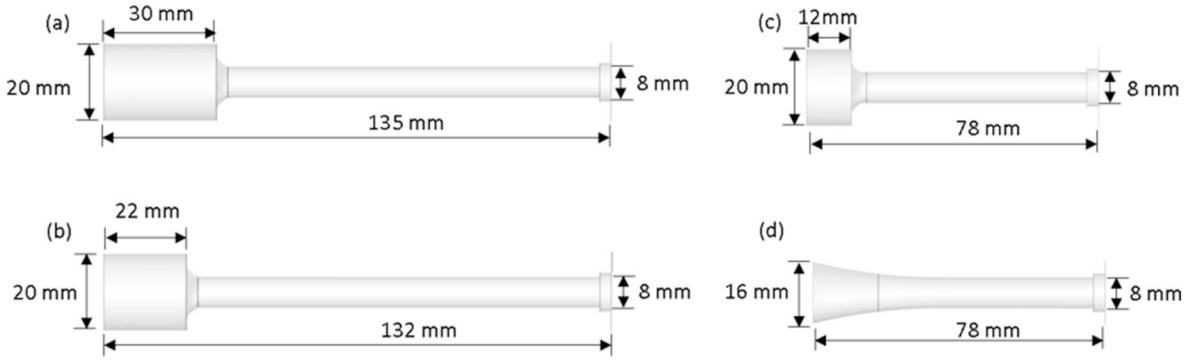

Fig. 1. (a), (b), (c) and (d): Dimensions of the SHVOF nozzles considered within this investigation (a) 30-135-8 nozzle, (b) 22-132-8 nozzle, (c) 12-78-8 nozzle, (d) 0-78-8 nozzle.

Table 1
Table of the boundary conditions employed within the model for all four nozzles.

		Temperature
Fuel flow rate	612 l/min	300 K
Oxygen flow rate	306 l/min	300 K
Suspension flow rate	50 ml/min	300 K
Initial droplet diameter and velocity	250 μm 30 m/s	300 K
Wall	No-slip	350 K

3. Model description

A fully structured 2-D axis-symmetric mesh is used to model the geometry. Fig. 1 (a), (b), (c) and (d) provides the dimensions for the nozzles. A description of the boundary conditions is given in Table 1 and Fig. 2, these conditions are within the range of typical operating conditions for a SHVOF thermal spray [15]. The gas phase is solved for using a QUICK scheme for the convective terms [5,16]. The suspension is injected using a two-way coupled discrete particle model [8] which considers the suspension droplets as a discrete entity moving through the continuous gas phase. The droplets are injected using a group injection comprising of two particle streams. This study was validated against a study by Mahrukh et al. on DJ2700 torch in reference [5]. The DJ700 torch modelled by Mahrukh et al. displayed an outlet velocity of 1900 m/s and an outlet temperature of 2350 K. The model employed within this study uses the same modelling technique as Mahrukh et al. for the gas phase. Using the same nozzle geometry for the DJ2700 torch, an outlet velocity of 1975 m/s and an outlet temperature of 2425 K were found which show good agreement between the results. The difference in the values was suspected to be due to some missing information about the dimensions of the injector, as well as the turbulence boundary conditions, which were not presented in that paper.

3.1. Gas modelling

To model the gas phase the following compressible governing equations are solved for; continuity, momentum conservation, ideal gas law, energy conservation, species fraction and the realizable k-ε turbulence model with the standard wall function. The underlying governing equations of the gas model have been omitted as there are many studies available in both modelling HVOF and SHVOF that present these [7,17,18].

3.1.1. Combustion model

Combustion is modelled using a species transport model and the eddy dissipation model [26] for both the hydrogen combustion and ethanol combustion. Information on the eddy dissipation model can be found in [16], it considers the transport of each of the individual species in the balanced chemical equation. For each individual species, the convection–diffusion equation is employed to model the species fraction. Hydrogen has been used for the fuel, at a temperature in excess of 2000 K the stable product from the complete combustion of hydrogen dissociate due to strong thermal vibrations. The combustion of hydrogen, which takes consideration of secondary species, is given by the global chemical Eq. (1). The coefficients can be determined via a chemical equilibrium Gordon and McBride [20].

$$n_1H_2 + n_2O_2 \rightarrow n_3H_2O + n_4OH + n_5O_2 + n_6O + n_7H_2 + n_8H \tag{1}$$

3.2. Suspension modelling

The Suspension is modelled using a two-way coupled Eulerian–Lagrangian model. The motion of the droplets is given by Newton's second law, Eq. (2). The significant force on particles is the drag forces and hence Eq. (2) reduces to Eq. (3). The drag coefficient, c_D, is given by the drag law determined by Crowe (Eq. (4)) [21] which considers the effect of the Mach number and the Reynolds number on the drag coefficient [12].

$$m_p\frac{du_p}{dt} = \sum F_p \tag{2}$$

$$m_p\frac{du_p}{dt} = \frac{1}{2}c_D\rho_g A_p(u_g - u_p)|u_g - u_p| \tag{3}$$

$$c_D = 2 + (C_{D0} - 2)e^{-3.07\sqrt{\gamma}\frac{1+Re(12.278+0.548\,Re)}{1+11.278\,Re}\frac{Ma}{Re}} + \frac{5.6/(1+Ma)}{\sqrt{\gamma}Ma}e^{-\frac{Re}{2Ma}} \tag{4}$$

A lumped capacitance approximation is used in determining the particle temperature, this assumption holds true for particles of Biot numbers no greater than 0.1 and assumes that internal temperature gradient of particles can be ignored. The particle temperature can be determined from Eq. (6). The heat transfer coefficient, h, is computed using the Ranz and Marshall [16] correlation given by Eq. (7).

$$Bi = \frac{Lh}{K} \tag{5}$$

$$(m\bullet c_p)_p\frac{dT_p}{dt} = hA_p(T_g - T_p) \tag{6}$$

$$Nu = \frac{hd_p}{K_\circ} = 2.0 + 0.6Re_d^{1/2}Pr^{1/3} \tag{7}$$

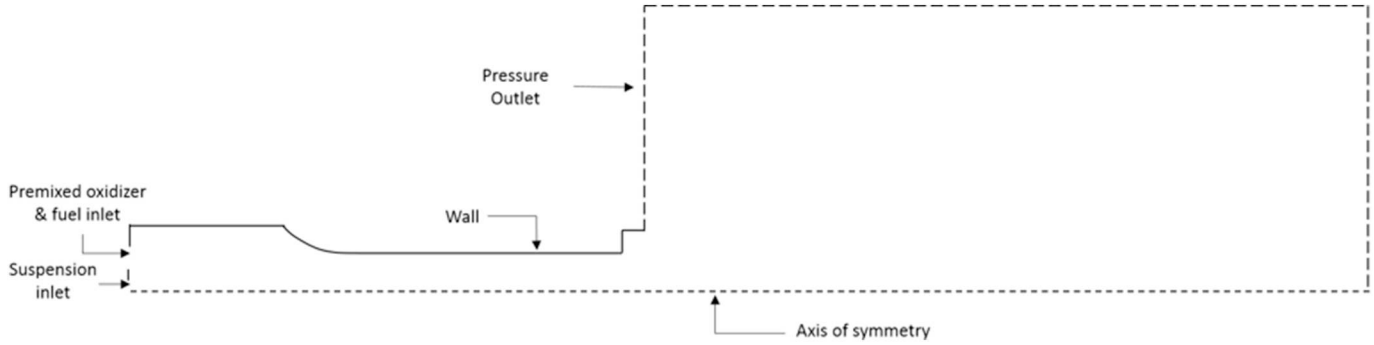

Fig. 2. Schematic of the 2-D axis-symmetric computational domain and boundary conditions.

Table 2
Thermo-physical properties; density, viscosity, specific heat and surface tension of ethanol [5].

Property	Ethanol temperature dependent functions	Temperature range (K)
Density (kg/m^3)	$\rho_l = aT^3 + bT^2 + cT + d$ $a = -3.76345 \times 10^{-6}$ $b = 2.27199 \times 10^{-3}$ $c = -1.2412$ $d = 1053.73$	250–385
Viscosity (kg/m·s)	$\mu_l = aT^3 + bT^2 + cT + d$ $a = 5.98 \times 10^{-10}$ $b = -4.87 \times 10^{-7}$ $c = 1.14 \times 10^{-4}$ $d = -5.50 \times 10^{-3}$	250–385
Specific heat (J/kg·K)	$c_l = aT^3 + bT^2 + cT + d$ $a = 4.42516 \times 10^{-5}$ $b = -6.58607 \times 10^{-4}$ $c = -3.03093$ $d = 2227.99$	250–385
Surface tension (N/m)	$\sigma_l = aT^6 + bT^5 + cT^4 + dT^3 + eT^2 + fT + g$ $a = -7.24434 \times 10^{-16}$ $b = 1.74074 \times 10^{-12}$ $c = -1.7235 \times 10^{-9}$ $d = 9.00117 \times 10^{-7}$ $e = -2.61702 \times 10^{-4}$ $f = 4.01095 \times 10^{-2}$ $g = -2.50259$	270–490

The properties of the suspension droplet are calculated from the individual constituents of the suspension; the suspension is comprised of ethanol and titania particles. This model neglects some of the complex physics within the suspension droplet such as Brownian motion, shell formations and the effect of particle morphology on the suspension droplet. The droplet specific heat, density, viscosity and surface tension are modified according to Eqs. (8), (9) and (10) respectively [22,23]. Eqs. (8)–(11) are implemented via UDFs within Ansys Fluent. Where the particle specific heat and density are given by c_{TiO2} is 690 J/kg·K and ρ_{TiO2} is 4230 kg/m^3 respectively. The liquid specific heat, density and viscosity are given by the polynomial functions found in Table 2. The functions were determined using experimental values and then curve fitted. Eq. (11) is used to determine the volume fraction of the particles within the suspension, the values of the mass fraction are calculated within the fluent solver for a multicomponent droplet and passed to the UDF to determine the volume fraction. The model employed within this study has used a similar technique to that of the study reported in reference [5]. In the mentioned study the thermal conductivity of the suspension was calculated and inputted into the ethanol properties. However, boiling laws require the thermal conductivity of the surrounding gas and not that of the suspension and as this model employs the volatile fraction the particle portion of the suspension is retained. This model also accounts for the effect that the change in composition of the suspension during boiling has on the properties of the suspension.

$$c_{susp} = Cc_{TiO_2} + (1 - C)c_l \tag{8}$$

$$\rho_{susp} = C\rho_{TiO_2} + (1 - C)\rho_l \tag{9}$$

$$\mu_{susp} = \mu_l\,(1 + 2.5C + 1.41C^2) \tag{10}$$

$$C = \frac{X_{i,TiO_2} m_{susp}/\rho_{TiO_2}}{m_{susp}/\rho_{susp}} \tag{11}$$

The model employed here incorporates a lower amount of volatile material within suspensions with higher particle concentrations which is modelled by Eqs. (13)–(16). The onset of droplet breakup can be characterised by Weber numbers greater than 14 and the droplet breakup is modelled using the TAB secondary breakup model [16]. This model has been extensively used within prior SHVOF modelling studies [12,24,25]. To model the evaporation the convection/diffusion controlled evaporation model has been employed [26] while also enabling the pressure dependent boiling and turbulence coupling options. The evaporation model is activated when the following criteria in Eqs. (13) and (14) are met, the evaporation rate is given by Eqs. (15) and (16).

$$We = \frac{\rho_\infty \Delta u^2 d}{\sigma} \tag{12}$$

$$T_{vap} \le T_p < T_{bp} \tag{13}$$

$$m_p > (1 - f_{v,0}) m_{p,0} \tag{14}$$

$$\frac{dm_p}{dt} = k_c A_p \rho \ln(1 + B_m) \tag{15}$$

$$B_m = \frac{Y_{i,s} - Y_{I,\infty}}{1 - Y_{i,s}} \tag{16}$$

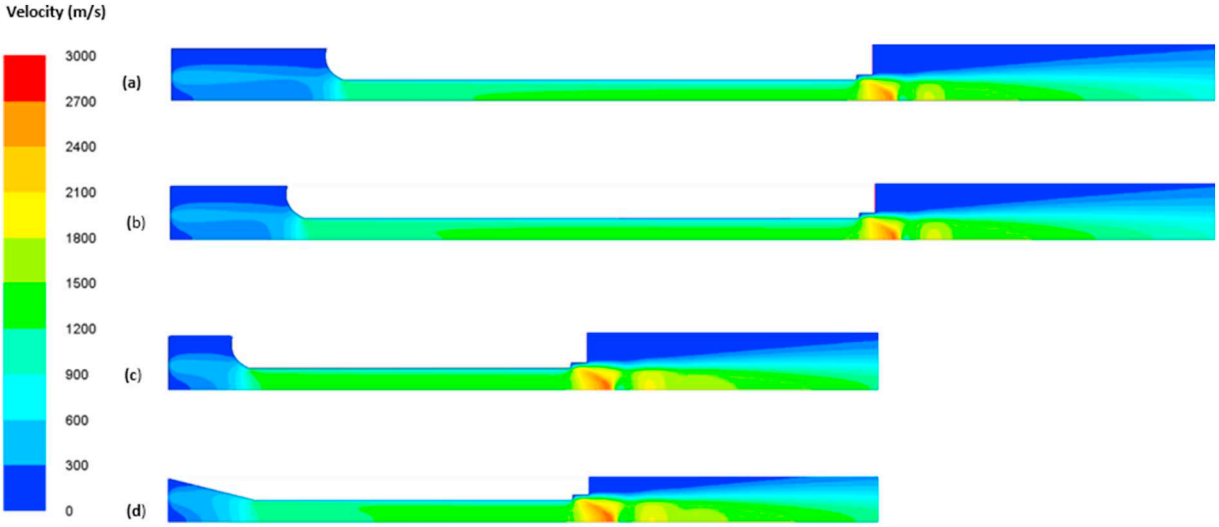

Fig. 3. (a), (b), (c) and (d): Contours of the gas velocity magnitude for the (a) 30-135-8 (b) 22-132-8 (c) 12-78-8 and (d) 0-78-8 nozzles before suspension injection.

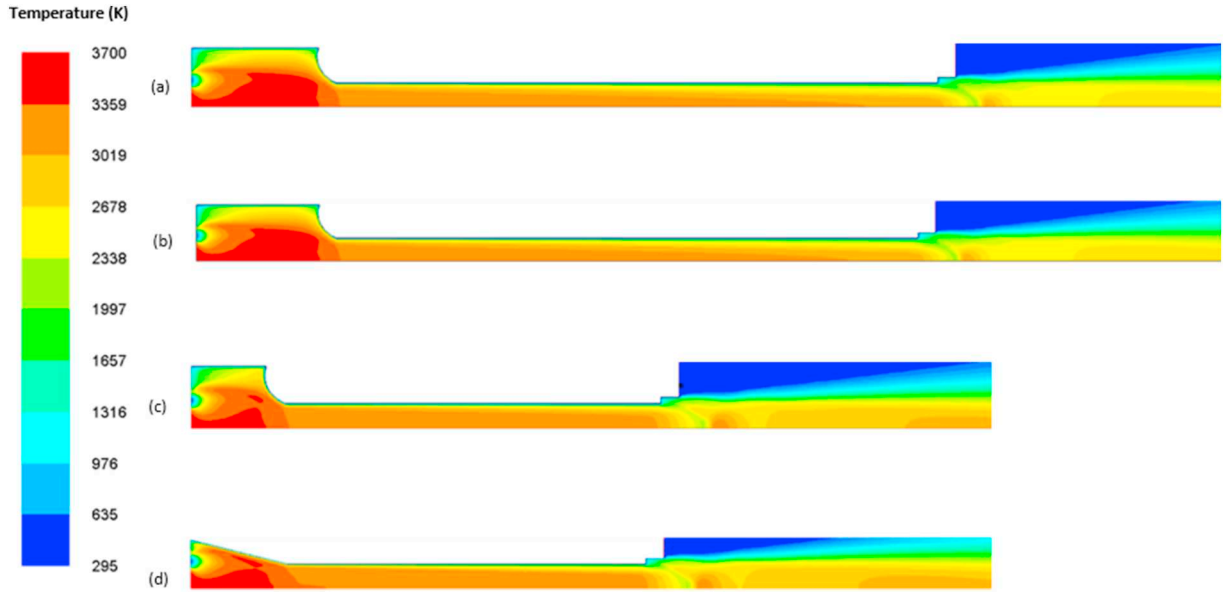

Fig. 4. (a), (b), (c) and (d): Contours of the gas temperature for the (a) 30-135-8 (b) 22-132-8 (c) 12-78-8 and (d) 0-78-8 nozzles before suspension injection.

4. Results and discussion

4.1. The effect of nozzle geometry on the gas dynamics

Figs. 3 and 4 compare the gas velocity magnitude and static temperature contours for the four nozzles. It can be seen that the shock waves have been resolved as the velocity magnitude contour demonstrates 3 shock diamonds. Figs. 5, 6 and 7 (a) and (b) show graphs comparing the centreline gas velocity magnitude, temperatures and pressures for the four nozzles under investigation respectively. From Fig. 5 (b) it is seen comparing the two longer nozzles, the 30-135-8 and the 22-132-8, to the two shorter nozzles, the 12-78-8 and 0-78-8, we can see prior to the nozzle exit before the shocks occur that the combustion gas exits the longer nozzles at a much higher velocity as opposed to the shorter nozzles. As the gas travels down the barrel it is accelerating, for nozzles with a longer barrel the duration the flow accelerates is greater. Hence for a longer barrel the gas velocity magnitude prior to the nozzle exit is greater. This is further demonstrated by comparing the two longest nozzles at the position −0.005 m. The 22 mm combustion chamber nozzle (22-132-8) has a barrel length of 110 mm and the 30 mm combustion chamber nozzle (30-135-8) has a barrel length of 105 mm. The gas enters the barrel of the two nozzles at approximately 1300 m/s for both nozzles; however, for the shorter barrel the flow exits at 2108 m/s and for the longer barrel the flow exits the barrel at 2133 m/s hence an increase in the barrel length of 5 mm has given an increase in the gas velocity of around 25 m/s. However, once the flow has exited the nozzle and expanded the gas velocity magnitude for the two 78 mm nozzles is around 150 m/s greater than the 30-135-8 and 22-135-8 nozzles. The reason for this is that the flow exiting the 78 mm nozzles is under-expanded to a greater degree than the 30-135-8 and the 22-132-8 nozzles. As the flow from the nozzles undergoes the succession of shock waves the flow from the 78 mm nozzles accelerates to a higher velocity than the 30-135-8 and 22-132-8 nozzles. Higher gas velocity typically translates to higher particle velocities which can result in denser coatings.

Fig. 6 (a) and (b) shows the static centreline temperature plots for all the nozzles. It can be seen that the maximum temperature within the nozzle exceeds typical flame temperatures of hydrogen. Studies modelling HVOF and SHVOF thermal spray have also found similar over predications from the combustion model [10,19]. The adiabatic flame temperature at assumed chamber pressure of 4 bar and equivalence ratio of 1.0 was calculated using software Gordan and McBride to be

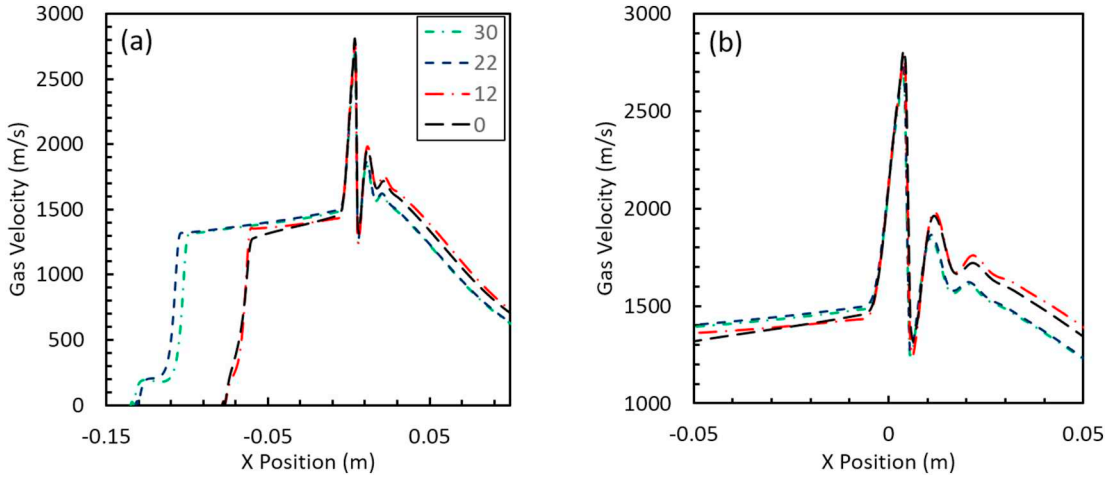

Fig. 5. (a) and (b): (a) Centreline gas velocity magnitude and (b) zoomed in velocity magnitude at the nozzle outlet without any suspension injection for the 30-135-8, 22-132-8, 12-78-8 and 0-78-8 nozzles.

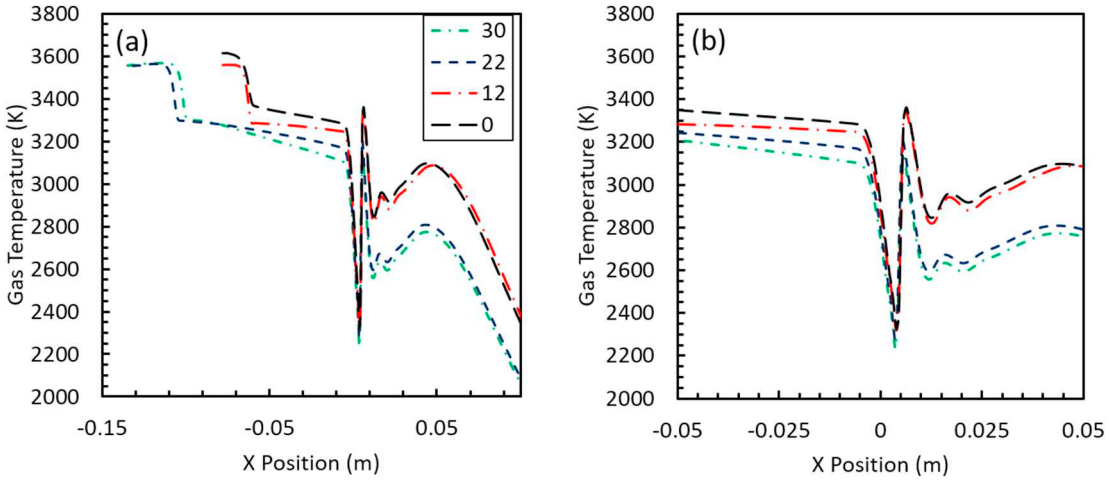

Fig. 6. (a) and (b): (a) Centreline gas static temperature and (b) zoomed in static temperature at the nozzle outlet without any suspension injection for the 30-135-8, 22-132-8, 12-78-8 and 0-78-8 nozzles.

3259 K. The model determines a temperature of 3556 K within the combustion chamber. There is an over prediction in the temperature of approximately 300 K, the over prediction results from determining the coefficients in Eq. (1). To accurately model the combustion reactions requires solving of typically 30 sub-reactions for hydrogen combustion and up to 300 reactions for hydrocarbon reactions. The simplification of this reaction into a one-step mechanism produces a source of error in the gas temperature. There are trace species that form such as H_2O_2 and HO_2, these intermediate species are not resolved using Gordan and McBride. Careful resolution of all reactions and species are very computationally expensive and hence affect the gas temperature. This one step mechanism along with the eddy dissipation model has been extensively used in SHVOF modelling including [26]. The gas exits the shorter 78 mm nozzles at a significantly higher temperature than the 30-135-8 and 22-132-8 nozzles. Preceding the nozzle exit, at the position of −0.005 m, the gas temperature for the 0-78-8 nozzle at around 400 K higher temperature than the 30-135-8 nozzle. This effect can also be seen comparing the 30-135-8 and 22-132-8 nozzles where the gas temperature for the latter nozzle is around 100 K higher temperature than the former nozzle. The reason for this is that the walls of the nozzles are cooled by an external water cooling system and this is allowed for in the model through a constant wall temperature boundary condition. The longer the nozzle the longer the duration of time the gas is cooled. Comparing the gas temperature plots to the literature [10,20,27] it can be seen that there is an unexpected increase in the gas temperature downstream of the nozzle exit. This increase in the gas temperature was also presented by Baik and Kim [28] for a HVOF simulation. The difference has been found to be due to the species fraction inlet condition. While specifying the species composition matching that of air at the inlet an increase in the gas temperature downstream of the nozzle exit is seen. This may be due to any unreacted H_2 reacting with the O_2 within the air. However, when one specifies a species composition of just N_2 at the inlet an increase is not observed. Hence the more physically representative inlet condition of air has been used within this study.

From Fig. 7 (a) and (b) it can be seen that the smaller the combustion chamber the higher the pressure is within the combustion chamber. As the flow travels down the barrel the frictional forces produce a pressure drop from the inlet of the barrel to the outlet of the barrel the longer the barrel the larger the pressure drops. This is demonstrated by comparing the 78 mm nozzles to the two remaining nozzles. The gas exiting the 78 mm nozzles exits at a static pressure of around 0.9 bar in contrast to the 135 mm nozzle which exits at a static pressure of around 0.75 bar.

In summary, one can see that the smaller combustion chamber results in a higher pressure within the combustion chamber and the

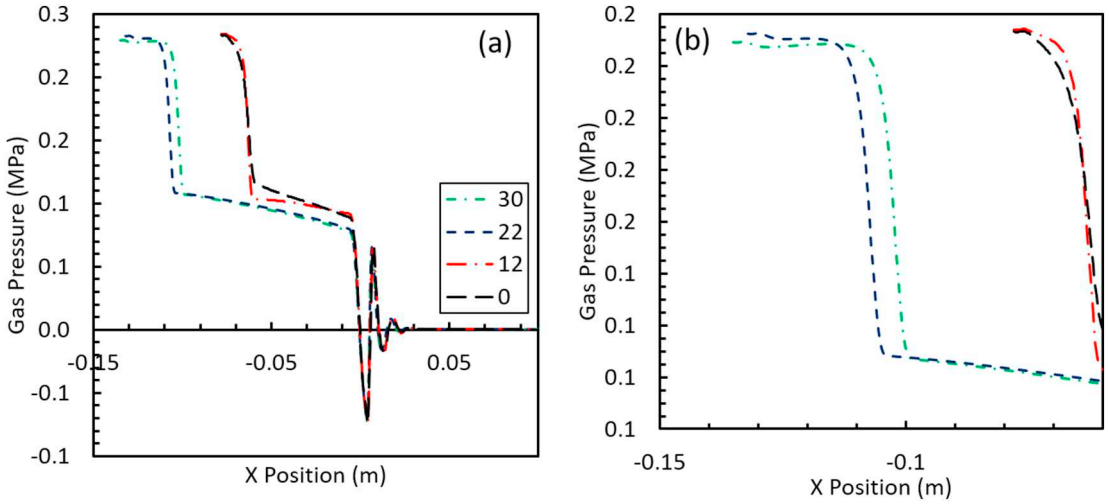

Fig. 7. (a) and (b): (a) Centreline gas static pressure and (b) zoomed static pressure at the nozzle outlet without any suspension injection for the 30-135-8, 22-132-8, 12-78-8 and 0-78-8 nozzles.

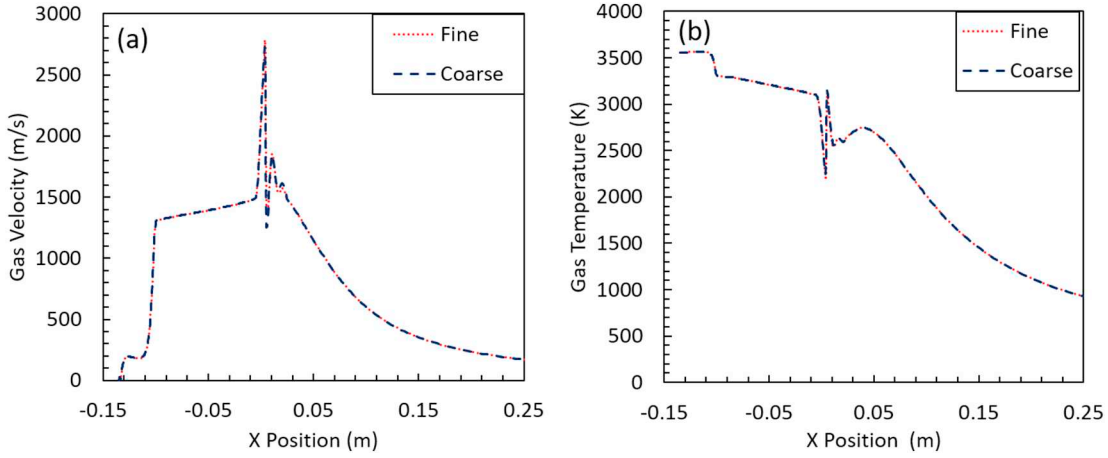

Fig. 8. (a), (b): Contours of the gas velocity and temperature for the 30-135-8 nozzle at different mesh resolutions.

longer barrel results in a higher velocity prior to the nozzle exit. However, with the shorter nozzle one sees a higher pressure prior to the nozzle outlet. Once the shorter nozzles have undergone the series of shocks one can see that the smaller nozzles operate at a higher gas velocity that the longer nozzles within the expanded free jet. The shorter nozzles operate at a higher gas temperature than the longer nozzles as the duration of contact of the gas with the cooled walls is much lower. To understand the effect that the gas properties has on the particles requires a model that is able to incorporate the particles within the suspension accurately. Which, current SHVOF thermal spray models are not yet able to capture due to the complexity of the underlying physics. From this one can better understand the link between gas velocity, temperature, suspension evaporation and residence time of particles within the nozzle has on the particle velocities and temperature which will allow for further control on the coating quality.

To ensure a mesh independent solution the mesh was refined in the region of the outlet. The cell spacing in the x and y direction were reduced by a factor of four within the nozzle and in the region of the shocks. In other regions the cell spacing was reduced by a factor of two. From Fig. 8 it can be seen comparing the coarse mesh and the fine mesh there is an identical solution which shows that the solution is mesh independent.

4.2. Effect of suspension concentration on the gas phase

Figs. 9 (a), 10 (a), 11 (a) and 12 (a) show that once the suspension has been injected there is a significant drop in the magnitude of gas velocity. The maximum drop in the velocity occurs within the throat of the nozzle with a drop in the gas velocity of approximately 1000 m/s. There is a drop in the gas velocity at the nozzle outlet of 300 m/s for the 78 mm nozzles and a drop in the gas velocity for the 132 mm and 135 mm nozzles of around 250 m/s. For all nozzle geometries it can be seen that the change in suspension composition has an insignificant effect on the gas velocity for suspension concentrations of 100% Ethanol to 75% Ethanol and 25% TiO_2 particles suspension. This too was seen in the model proposed Mahrukh et al. [5] for the DJ2700 HVOF thermal spray nozzle with suspension. The change in suspension concentration from 100% ethanol to 75% ethanol and 25% TiO_2 showed little to no effect on the centreline gas velocity for a constant s.

From Figs. 9 (b), 10 (b), 11 (b) and 12 (b) show that the temperature drops significantly once the suspension has been injected. For all four nozzles as the particle concentration increases within the suspension, the temperature drop within the nozzle throat decreases while comparing the gas temperature with the suspension injection to that of no suspension injection. For instance, the 30-135-8 nozzle has a minimum

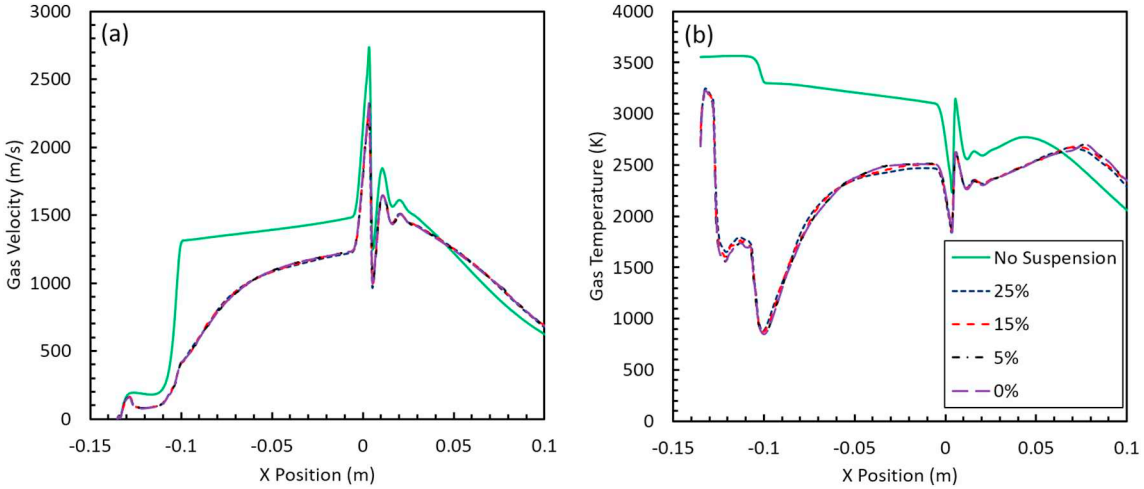

Fig. 9. (a) and (b): Centreline gas velocity (a) and static gas temperature (b) for the 30-135-8 nozzle with no suspension injected and varying suspension concentrations from 0% TiO_2 to 25% TiO_2.

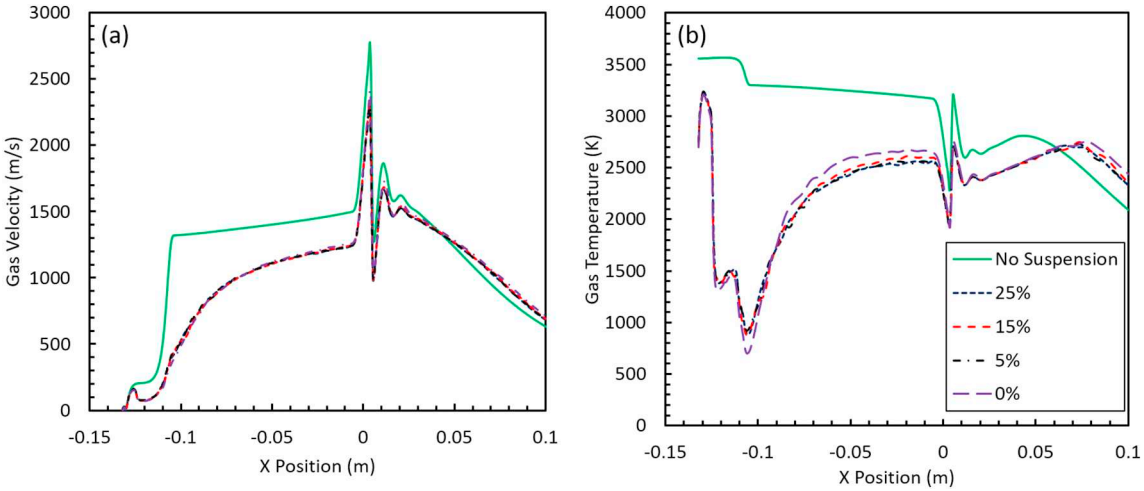

Fig. 10. (a) and (b): Centreline gas velocity (a) and static gas temperature (b) for the 22-132-8 nozzle with no suspension injected and varying suspension concentrations from 0% TiO_2 to 25% TiO_2.

temperature of 895 K for the 75% ethanol and 25% TiO_2 suspension. For the 100% ethanol suspension there is a minimum gas temperature within the nozzle throat of 849 K. Similarly, as the gaseous ethanol combusts heat is returned to the system and for suspensions with a lower particle concentration the centreline gas temperature is higher than that of suspensions with a higher particle concentration. At the nozzle outlet the centreline gas temperature is 158 K higher for a pure ethanol suspension injection to that of a 75% ethanol and 25% TiO_2 suspension injection for the 0-78-8 nozzle.

Figs. 12 and 13 show the effect of modelling the volatile faction and the properties as a function of the composition of suspension droplets for the gas velocity and temperature on the 0-78-8 nozzle. Comparing Figs. 12 (a) and 13 (a) it can be seen that there is not a significant effect that this modelling approach used within this study has on the gas velocity. However, comparing Figs. 12 (b) and 13 (b) there is a difference in the centreline temperature plots especially as the particle concentration increases. Using this model for a 25% particle concentration within the suspension the gas temperature reaches a minimum value of 1000 K. However, while one neglects the volatile fraction and the effect that the evaporation of ethanol has on the specific heat and density in particular within the model the minimum gas temperature reaches 1300 K. At the nozzle outlet one can also see a difference of 100 K while comparing Figs. 12 and 13. It can also be seen that at around 0.1 m from the outlet there is a difference of 200 K when one neglects to model the volatile fraction and the change in the properties during evaporation of the suspension. Hence there is an observable difference in the gas temperature while including the volatile fraction of the suspension droplets which many SHVOF thermal spray studies have neglected. As the ethanol reacts, heat is recuperated back into the system. With suspension comprising of high particle concentrations neglecting to model the volatile fraction results in an over prediction in the gas temperature.

In summary, comparing the nozzles with a length of 78 mm to 135 mm or 132 mm: 0-78-8, 12-78-8, 30-135-8 and 22-132-8 nozzles respectively, it can be seen there is a larger decrease in the gas velocity for the 78 mm nozzles at the nozzle outlet. The suspension concentration has little effect on the gas velocity. However, one can see that the suspension concentration has a notable effect on the gas temperature while modelling the suspension with the added volatile fraction of the droplets. The lower particle concentrations result in a higher temperature drop within the nozzle throat; the region where the combustion chamber meets the barrel. Higher particle concentrations also result in a lower gas temperature towards the exit of the nozzle. Finally, the higher particle concentration results in a lower gas temperature

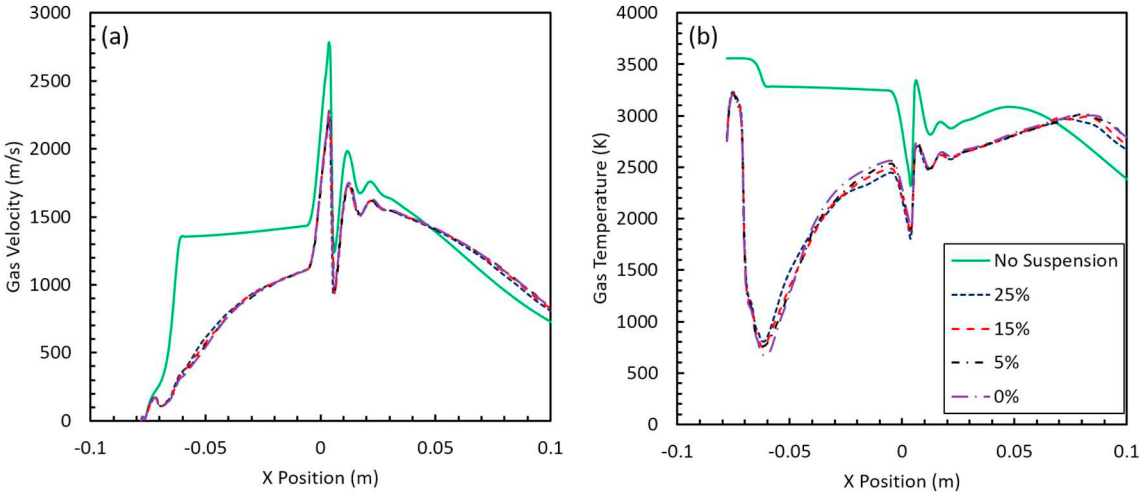

Fig. 11. (a) and (b): Centreline gas velocity (a) and static gas temperature (b) for the 12-78-8 nozzle with no suspension injected and varying suspension concentrations from 0% TiO_2 to 25% TiO_2.

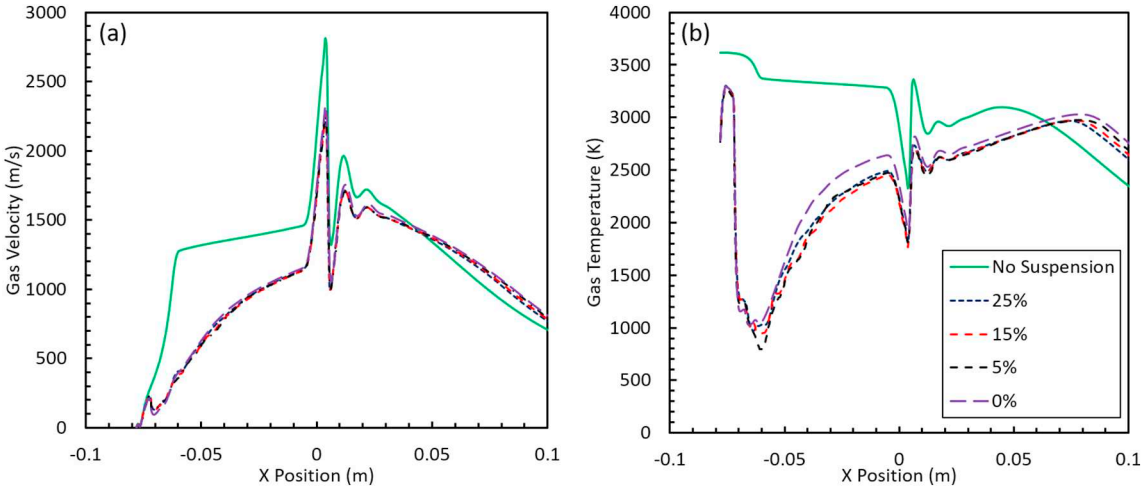

Fig. 12. (a) and (b): Centreline gas velocity (a) and static gas temperature (b) for the 0-78-8 nozzle with no suspension injected and varying suspension concentrations from 0% TiO_2 to 25% TiO_2.

downstream from the nozzle outlet due to a lower availability of ethanol available to combust and provide additional energy to the system. With a model that allows for the particle velocities and temperatures to be determined more accurately one can choose a particle concentration to carefully control the temperature drop within the nozzle. Such that the temperature drop, once the suspension has been injected does not adversely affect the overall quality of the coating.

4.3. Effect of nozzle geometry and suspension concentration on suspension evaporation

Fig. 14 shows the evaporation rates for the 30-135-8, 22-132-8, 12-78-8 and 0-78-8 nozzles respectively with varying particle concentrations within the suspension. The most significant factor affecting the evaporation of suspension vaporization is the nozzle length. It is seen from Fig. 14 with the 78 mm length nozzles, the suspension vaporization continues close to the nozzle exit. For the SHVOF thermal spray process it is desired that the suspension vaporizes as soon as possible to release the particles into the gas stream. This allows for maximum duration of time that the particles are heated and accelerated allowing for particles to impact the substrate at a higher velocity and in their molten state. Therefore, for a given standoff distance and materials with a high melting point would benefit from using the nozzles with a length of 135 mm or 132 mm as opposed to the 78 mm nozzles. This will result in better adhesion of the coating to the substrate due to the higher degree of melting particles impacting the substrate.

From Fig. 14 it can be seen that the maximum evaporation rate decreases as the concentration of TiO_2 particles increases within the suspension. The lower amount of ethanol within the suspension, due to the lower availability of ethanol a lower evaporation rate can be seen. It can also be seen for the 30 mm, 22 mm and 12 mm nozzles in Fig. 14, as the combustion chamber size increases the maximum rate of evaporation of the suspension decreases. It can be seen that the location of the maximum evaporation occurs within the throat of the nozzle where the pressure is lower. In the studies by Dongmo et al. and Taleby and Hossainpour a similar nozzle to the 22-132-8 nozzle was modelled it was also seen with these studies that the maximum evaporation occurs within the throat region of the nozzle [7,10]. For nozzles with a larger combustion chamber the throat is located further from the nozzle inlet therefore more of the suspension has been vaporized before the suspension has travelled to the throat. Therefore, it can be seen that a lower evaporation rate at the throat due to the lower availability of liquid within the suspension at the throat of the nozzle. Fig. 15 (a), (b), (c) and (d) shows the evaporation rate at the nozzle centreline for a

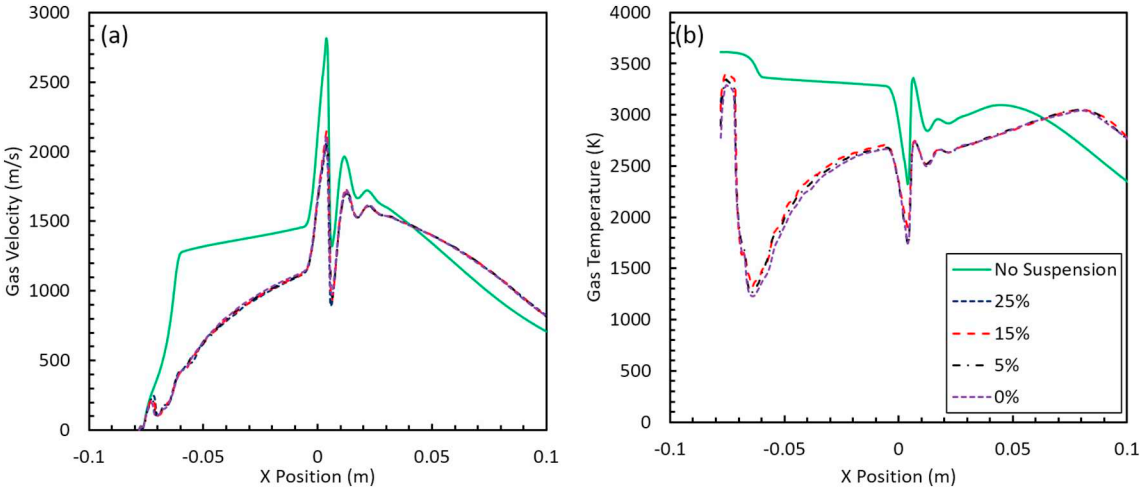

Fig. 13. (a) and (b): Centreline gas velocity (a) and static gas temperature (b) for the 0-78-8 nozzle with no suspension injected and varying suspension concentrations from 0% TiO_2 to 25% TiO_2 without modelling the volatile fraction.

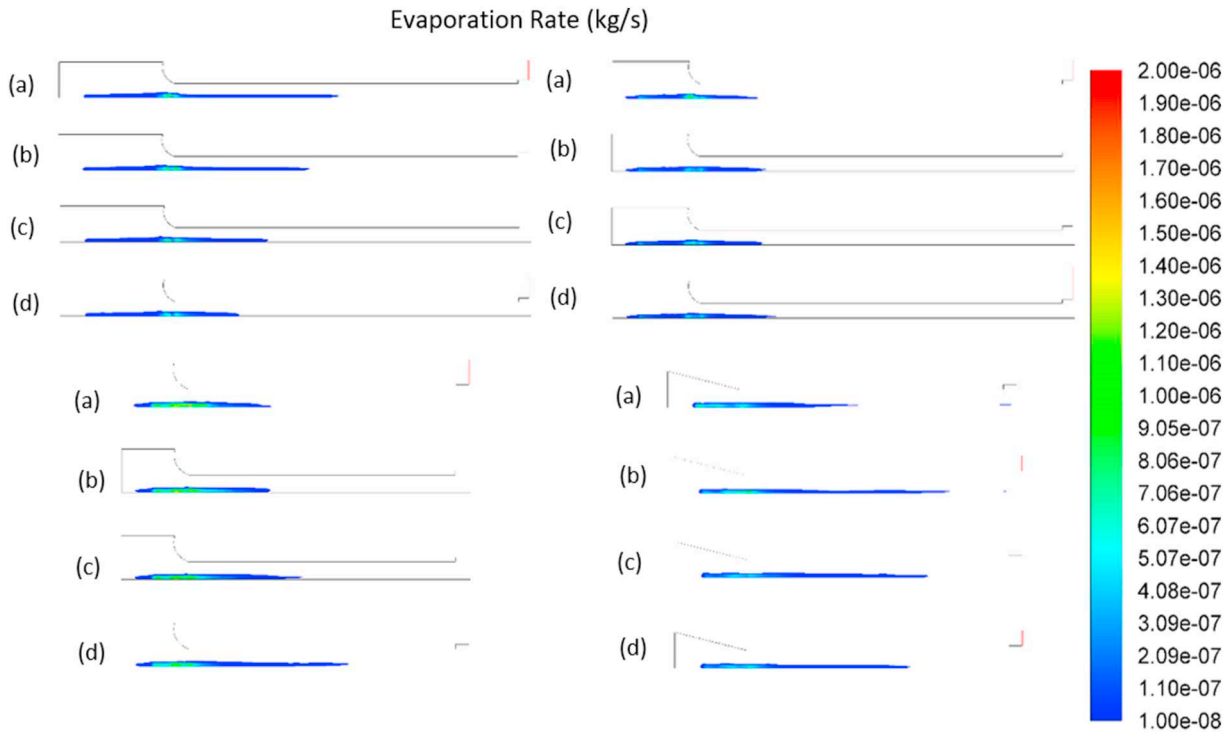

Fig. 14. Contours of the evaporation rate for the (top left) 30-135-8 nozzle, (top right) 22-132-8 nozzle, (bottom left) 12-78-8 nozzle and (bottom right) 0-78-8 nozzle for suspension concentrations of (a) 100% ethanol, (b) 95% ethanol, (c) 85% ethanol and (d) 75% ethanol suspension.

100% ethanol, 95% ethanol, 85% ethanol and 75% ethanol suspension. It is further demonstrated that the smaller the combustion chamber the higher the evaporation rate is within the nozzle centreline.

From the study conducted by Mahrukh et al. [5] it was seen that for suspensions with higher concentrations of particles, the final location of droplet vaporization occurs further downstream from the nozzle inlet. Here it can be seen that for suspensions with a higher particle concentration the final location of evaporation moves towards the nozzle inlet. The discrepancy in the two observations may be attributed to modelling the volatile fraction and neglecting to model the change in suspension properties as ethanol evaporates from the suspension. For suspensions with a high particle concentration there is a lower availability of vaporizable material for a fixed flow rate. Hence despite the higher specific heat of this suspension, vaporization commences sooner than suspensions with a higher particle concentration as seen in Fig. 14.

In summary suspension vaporization is influenced by the nozzle length; unlike the 135 mm and 132 mm nozzles in the 78 mm length nozzles the suspension vaporization commences closer to the nozzle exit. The maximum evaporation rate decreases as the concentration of TiO_2 particles increases within the suspension. This can be attributed to the lower availability of ethanol within the suspension. One can also see a lower maximum evaporation rate within nozzles that have a larger combustion chamber at the nozzle throat. With the suspension vaporizing more readily the particles are released into the combustion gasses sooner which extends the residence time of particle acceleration and heating. This allows for particles to be accelerated to higher velocities and heated to higher temperatures which results in denser higher quality coating.

5. Conclusions

This study has investigated the effect of the nozzle geometry on the gas velocity, temperature and pressure. In addition, this study has investigated the effect of the particle concentration within the suspension on the gas velocity and temperature and this work has progressed SHVOF thermal spray modelling by including the volatile fraction of the droplets within the model. The results from the model incorporating the volatile fraction are compared to the model without it. From this study it can be seen that the nozzle geometry has a notable impact on the gas dynamics and the evaporation rate. The following conclusions can be drawn:

- Comparing the gas dynamics across the four nozzles it can be concluded that the smaller combustion chamber results in a higher pressure within the combustion chamber while shorter nozzles see a higher pressure at the nozzle outlet. Longer barrels result in a higher velocity prior to the nozzle exit (within the barrel) while smaller nozzles operate at a higher gas velocity than the longer nozzles within the region free jet beyond the shock diamonds. The shorter the nozzle length the higher the gas temperature as the duration of contact of the gas with the cooled walls is much smaller.
- Comparing the nozzles with various lengths we see a larger decrease in the gas velocity for the 78 mm nozzles at the nozzle outlet. The suspension concentration has negligible effect on the gas velocity. However, the concentration of the suspension affects the gas temperature; the lower particle concentrations result in a higher temperature drop within the throat of the nozzle in comparison to the gas temperature before suspension is injected. Higher particle concentrations also result in a lower gas temperature towards the nozzle exit as well as a lower gas temperature downstream from the nozzle exit due to as lower amount of ethanol combustion. For the SHVOF thermal spray process the aim is to maximise the particle temperature and velocity prior to impact on the substrate. Typically, higher particle velocity and temperatures are seen from higher gas velocity and temperature.
- Evaporation of suspension vaporization is influenced by the nozzle length, unlike the 135 mm and 132 mm nozzles in the two 78 mm length nozzles the suspension vaporization commences closer to the nozzle exit. The larger combustion chamber results in a lower maximum evaporation rate within the nozzle. The maximum evaporation rate decreases as the concentration of TiO_2 particles increases within the suspension due to the higher specific heat of the suspension.

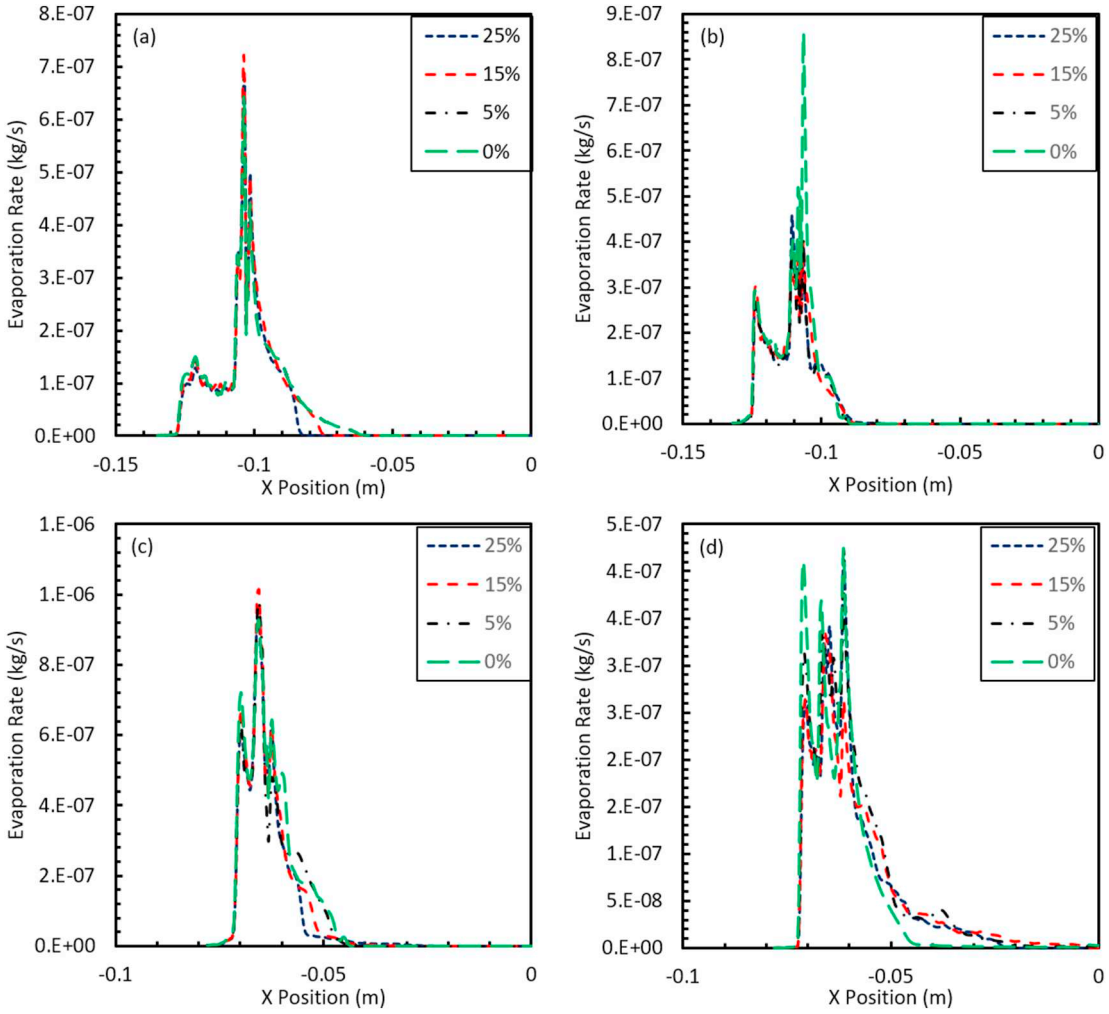

Fig. 15. (a), (b), (c) and (d): Plots of evaporation rate in kg/s for the four nozzles at varying suspension concentrations (a) 100% ethanol suspension, (b) 95% ethanol suspension, (c) 85% ethanol suspension and (d) 75% ethanol suspension.

Nomenclature

A	area
B_m	Spalding mass number
C	volume fraction
c_D	drag coefficient
c_p	specific heat
F	force
h	heat transfer coefficient
K	thermal conductivity
$\dot{m}$	mass flow rate
m	mass
ρ	density
T	temperature
t	time
u	velocity
X	mass fraction
x	displacement
μ	dynamic viscosity
σ	surface tension
γ	ratio of specific heats
Y	vapor mass fraction

Subscript

d	particle at diameter d
g	gas
i	ith species
p	particle
s	value at droplet surface
o	bulk gas
TiO_2	titanium dioxide

Non-dimensional parameters

Bi	Biot number
Ma	Mach number
Pr	Prandtl number
Re	Reynolds number
Sc	Schmidt number
Sh	Sherwood number
We	Weber number

Acknowledgment

This work was supported by the Engineering and Physical Sciences Research Council [EP/N50970X/1]. Access to high performance computing resources provided by the University of Nottingham is gratefully acknowledged.

References

[1] M. Bai, Z. Pala, T. Hussain, Microstructure and phase stability of suspension high velocity oxy-fuel sprayed yttria stabilised zirconia coatings from aqueous and ethanol based suspensions, J. Eur. Ceram. Soc. 38 (2017) 1878–1887.

[2] R. Gadow, A. Killinger, J. Rauch, Introduction to high-velocity suspension flame spraying (HVSFS), J. Therm. Spray Technol. 17 (2008) 655–661.

[3] M. Bai, R. Khammas, L. Guan, J.W. Murray, T. Hussain, Suspension high velocity oxy-fuel spraying of a rutile TiO2 feedstock: microstructure, phase evolution and photocatalytic behaviour, Ceram. Int. 43 (2017) 15288–15295.

[4] H. Tabbara, S. Gu, A study of liquid droplet disintegration for the development of nanostructured coatings, AICHE J. 58 (2012) 3533–3544.

[5] M. Mahrukh, A. Kumar, S. Gu, S. Kamnis, E. Gozali, Modeling the effects of concentration of solid nanoparticles in liquid feedstock injection on high-velocity suspension flame spray process, Ind. Eng. Chem. Res. 55 (2016) 2556–2573.

[6] M. Mahrukh, A. Kumar, S. Gu, Effects of angular injection, and effervescent atomization on high-velocity suspension flame spray process, Surf. Coat. Technol. 302 (2016) 368–382.

[7] E. Dongmo, R. Gadow, A. Killinger, M. Wenzelburger, Modeling of combustion as well as heat, mass, and momentum transfer during thermal spraying by HVOF and HVSFS, J. Therm. Spray Technol. 18 (2009) 896–908.

[8] E. Dongmo, A. Killinger, M. Wenzelburger, R. Gadow, Numerical approach and optimization of the combustion and gas dynamics in High Velocity Suspension Flame Spraying (HVSFS), Surf. Coat. Technol. 203 (2009) 2139–2145.

[9] M. Jadidi, S. Moghtadernejad, A. Dolatabadi, Numerical simulation of primary breakup of round non-turbulent liquid jets in shear laden gaseous crossflow, At. Sprays. 27 (2017) 227–250.

[10] M. Taleby, S. Hossainpour, Numerical investigation of high velocity suspension flame spraying, J. Therm. Spray Technol. 21 (2012) 1163–1172.

[11] M. Jadidi, A.Z. Yeganeh, A. Dolatabadi, Numerical study of suspension HVOF spray and particle behavior near flat and cylindrical substrates, J. Therm. Spray Technol. (2017) 1–14.

[12] M. Jadidi, S. Moghtadernejad, A. Dolatabadi, Numerical modeling of suspension HVOF spray, J. Therm. Spray Technol. 25 (2016) 451–464.

[13] M. Jadidi, S. Moghtadernejad, A. Dolatabadi, A comprehensive review on fluid dynamics and transport of suspension/liquid droplets and particles in high-velocity oxygen-fuel (HVOF) thermal spray, Coatings 5 (2015) 576–645.

[14] M. Oksa, E. Turunen, T. Suhonen, T. Varis, S.-P. Hannula, Optimization and characterization of high velocity oxy-fuel sprayed coatings: techniques, materials, and applications, Coatings. 1 (2011) 17–52.

[15] Z. Pala, E. Shaw, J. Murray, N. Senin, T. Hussain, Suspension high velocity oxy-fuel spraying of TiO2: a quantitative approach to phase composition, J. Eur. Ceram. Soc. 37 (2016) 801–810.

[16] I. Ansys, ANSYS FLUENT theory guide, Knowl. Creat. Diffus. Util. 15317, 2009, pp. 724–746.

[17] E. Dongmo, M. Wenzelburger, R. Gadow, Analysis and optimization of the HVOF process by combined experimental and numerical approaches, Surf. Coat. Technol. 202 (2008) 4470–4478.

[18] J. Pan, S. Hu, L. Yang, K. Ding, B. Ma, Numerical analysis of flame and particle behavior in an HVOF thermal spray process, Mater. Des. 96 (2016) 370–376.

[19] S. Kamnis, S. Gu, Numerical modelling of propane combustion in a high velocity oxygen–fuel thermal spray gun, Chem. Eng. Process. Process Intensif. 45 (2006) 246–253.

[20] P.D.C. Mingheng Li, Multi-scale modeling and analysis of an industrial HVOF thermal spray process, Chem. Eng. Sci. 60 (2005) 3649–3669.

[21] C.T. Crowe, Drag coefficient of particles in a rocket nozzle, AIAA J. 5 (1967) 1021–1022.

[22] E. Gozali, M. Mahrukh, S. Gu, S. Kamnis, Numerical investigation on effects of nanoparticles on liquid feedstock behavior in High Velocity Oxygen Fuel (HVOF) suspension spraying, Surf. Coat. Technol. (2015) 370–377.

[23] A. Farrokhpanah, T. Coyle, J. Mostaghimi, Numerical study of suspension plasma spraying, J. Therm. Spray Technol. 26 (2017) 12–36.

[24] M. Mahrukh, A. Kumar, S. Gu, S. Kamnis, Computational development of a novel aerosol synthesis technique for production of dense and nanostructured zirconia coating, Ind. Eng. Chem. Res. 55 (2016) 7679–7695.

[25] E. Gozali, S. Kamnis, S. Gu, Numerical investigation of combustion and liquid feedstock in high velocity suspension flame spraying process, Surf. Coat. Technol. 228 (2013) 176–186.

[26] E. Gozali, M. Mahrukh, S. Gu, S. Kamnis, Numerical analysis of multicomponent suspension droplets in high-velocity flame spray process, J. Therm. Spray Technol. 23 (2014) 940–949.

[27] M. Li, P.D. Christofides, Modeling and control of high-velocity oxygen-fuel (HVOF) thermal spray: a tutorial review, J. Therm. Spray Technol. 18 (2009) 753–768.

[28] J.-S. Baik, Y.-J. Kim, Effect of Nozzle Shape on the Performance of High Velocity Oxygen-fuel Thermal Spray System, (2008), pp. 5457–5462.